Nanoscale

PAPER

View Article Online
View Journal

Check for updates

Cite this: DOI: 10.1039/d6nr01376g

High-temperature molecular beam epitaxy of hexagonal boron nitride monolayers on carbon nanotubes

Jonathan Bradford, *†[a] William. J. Cull, †[b] Tin S. Cheng,[a] Amy F. M. Collins,[a] Christopher J. Mellor,[a] Andrei N. Khlobystov, [b] Alexandre Gloter,[c] Alexandra Ibanez,[d] Bernard Gil,[d] Pierre Valvin,[d] Guillaume Cassabois,[d,e] Alberto Zobelli[c] and Sergei V. Novikov*[a]

Received 7th April 2026,
Accepted 15th May 2026

DOI: 10.1039/d6nr01376g

rsc.li/nanoscale

We report the growth of hexagonal boron nitride (hBN) layers on multiwalled carbon nanotubes (MWCNTs) by high-temperature molecular beam epitaxy (HT-MBE). Using a variety of characterisation techniques, including transmission electron microscopy (TEM) and aberration-corrected scanning transmission electron microscopy combined with electron energy loss spectroscopy (AC-STEM-EELS), we demonstrated the epitaxy of boron nitride on the external surfaces of MWCNTs. This process formed coaxial heterostructures consisting of an inner multiwalled carbon nanotube coated with a few monolayers of hBN. The high structural quality of the carbon surface of the MWCNTs enabled smooth, uniform deposition of several monolayers of hBN. We proposed nucleation at defects on the MWCNT surface, followed by a step-flow-like "wrapping" mechanism for the hBN epitaxy around the carbon nanotubes. Additionally, boron nitride nanotubes grew from the open step edges at the tips of the multiwalled carbon nanotubes, facilitating the formation of circular carbon nanotube – boron nitride nanotube (BNNT) heterojunctions. Spatially-resolved photoluminescence (PL) spectroscopy in the UV-C spectral range confirmed the excellent structural quality of the hBN monolayers on the CNTs. The PL spectrum of BNNTs exhibited a line around 5.8 eV, which corresponds to the phonon replica in bulk hBN associated with phonon-assisted recombination involving optical phonons. This PL spectrum provides the first evidence of intrinsic radiative exciton recombination in quasi-one-dimensional hBN, with an estimated indirect bandgap of approximately 5.95 eV.

1. Introduction

There has been a surge of interest in hexagonal boron nitride (hBN) due to its technological potential for deep ultraviolet (DUV) photonics,[1,2] single-photon emitters (SPEs),[3,4] and its incorporation into van der Waals (vdW) two-dimensional (2D) heterostructures.[5,6] Hexagonal boron nitride has only a small ~1.7% lattice mismatch to graphene and that makes it an ideal dielectric for use in graphene-based devices.[6]

We have developed high-temperature molecular beam epitaxy (HT-MBE) of hBN at growth temperatures from 1100 °C to 1700 °C, using high-temperature sublimation and e-beam MBE sources for boron and nitrogen, and RF-plasma sources.[7–10] We have demonstrated a direct optical energy gap of ~6.1 eV (ref. 11 and 12) and an electronic band gap of ~6.8 eV (ref. 13 and 14) in a single monolayer hBN grown on highly ordered pyrolytic graphite (HOPG) substrates. We have shown that the single-photon emitters in hBN layers can be reproducibly grown by HT-MBE using carbon doping.[15]

Recent studies worldwide have focused on developing novel 2D lateral heterostructures with unique transport and optical properties. Whereas vertical 2D heterostructures can be produced by epitaxy or by exfoliating and stacking 2D layers, lateral 2D heterostructures can only feasibly be produced by an epitaxial growth process. In sequential HT-MBE growth of hBN, graphene and a second cycle of hBN growth we were able to achieve lateral hBN–graphene–hBN heterostructures, in which a strip of graphene is laterally embedded between monolayers of hBN.[9,16]

---

[a] *School of Physics and Astronomy, University of Nottingham, Nottingham NG7 2RD, UK. E-mail: jonathan.bradford@nottingham.ac.uk, sergei.novikov@nottingham.ac.uk*
[b] *School of Chemistry, University of Nottingham, Nottingham, NG7 2RD, UK*
[c] *Université Paris-Saclay, CNRS, Laboratoire de Physiques des Solides, 91405 Orsay, France*
[d] *Laboratoire Charles Coulomb, UMR5221 CNRS-Université de Montpellier, 34095 Montpellier, France*
[e] *Institut Universitaire de France, 75231 Paris, France*

† These authors contributed equally.

Another promising direction in the growth and physics of low-dimensional materials is research into boron nitride and carbon nanotubes (BNNTs and CNTs, respectively) (ref. 17 and references therein). Nanoscale electronic devices constructed from nanotubes are of particular interest due to their unique form factor (two nanoscale dimensions and one macroscale dimension), which enables the creation of wire-like structures with physical properties markedly different from those of their 2D analogues.[18] Additionally, the curved internal and external surfaces of these nanotubes can provide a platform for further functionalization, templating the growth of nanomaterials with unique optical[19] and electronic properties,[20] novel structural configurations,[21] and enhanced catalytic activities.[22] We have previously demonstrated that the thermal treatment of fullerenes confined within BNNTs allows for the formation of CNTs inside BNNTs, affording a hybrid nanostructure to form the world's smallest coaxial cable.[23]

Here, we explore HT-MBE as a route to forming heterostructures of CNTs and BNNTs, considering the feasibility of deposition on the external and internal surfaces, as well as the opened tips of multiwalled (MW) CNTs. Structural and elemental mapping of the nanotubes shows preferential formation hBN layers on the external surfaces of the nanotubes forming few-layer hBN/MWCNT coaxial heterostructures. We also observe growth from the open tips of the MWCNTS facilitating the growth of lateral BNNT-MWCNT heterojunctions. We study the optical properties of the layers in the UV-C range by spatially resolved photoluminescence spectroscopy, providing the first evidence of intrinsic radiative exciton recombination in quasi-one-dimensional hBN.

2. Experimental methods

2.1. High-temperature molecular beam epitaxy

Multiwall carbon nanotubes were purchased from NANOLAB (PD30 multiwalled (MW) carbon nanotubes (CNTs), synthesised by chemical vapour deposition (CVD)). Before use, the PD30 MWCNTs (60 mg) were refluxed in concentrated nitric acid (20 mL, 83 °C, 3 h) to remove Fe catalyst, residual amorphous carbon and to open nanotube end caps. The reaction mixture was then diluted with water (1 L) and filtered through a PTFE membrane filter (pore size 200 nm) to obtain cleaned, open PD30 MWCNTs (48 mg) as a black powder.

Boron nitride layers were grown on carbon nanotubes drop cast onto 10×10 mm^2 c-plane sapphire wafers using a custom-designed Veeco GENxplor MBE system capable of achieving growth temperatures as high as 1850 °C under ultra-high-vacuum conditions. Details of the HT-MBE growth of hBN have been published previously.[9,10,16] In all our studies, we relied on thermocouple readings to determine the substrate's growth temperature. For all samples discussed in the current paper the growth temperature was about 1390 °C with growth times of 2 to 4 hours. Substrates rotated at 5 rpm during the epitaxial process to ensure uniform coverage across the sample. We used a high-temperature Knudsen effusion cell (Veeco) to evaporate boron. Boron has two naturally occurring stable isotopes, the natural mixture contains 11B (80.1%) and 10B (19.9%). In these studies, we used isotopically enriched (96%) boron 10B with 5N purity.[10] We used a conventional Veeco RF-plasma source to provide the active nitrogen flux with RF-power of 550 W and a N_2 flow rate of 2 sccm. These conditions have been chosen based on optimised growth of hBN on HOPG substrates.[9] We expect that during HT-MBE, boron nitride will grow on the surface of sapphire substrates as it does on the surface of multiwalled carbon nanotubes.

2.2. Characterisation

2.2.1. Transmission electron microscopy (TEM). To study the structural properties of the grown boron nitride layers, TEM imaging was conducted using a JEOL 2100F FEG-TEM microscope operated at 200 kV. Samples were mounted onto TEM grids using dry deposition methods (*i.e.* lightly pressing TEM grids onto the MBE-grown sample) or drop casting (scraping the sample off the sapphire and sonicating in isopropyl alcohol, followed by drop casting). Lacey-carbon-coated TEM grids from Agar Scientific were used for TEM imaging. EDX analysis was performed using an Oxford Instruments XMax 80 X-ray microanalysis system on a JEOL 2100F FEG-TEM. Uncorrected STEM-EELS analysis was performed using a Gatan Enfinium SE spectrometer on a JEOL 2100 plus microscope at 200 kV. STEM-EELS data was denoised using a Savitzky–Golay smoothing filter (second order, 10 points).

To achieve atomic-scale chemical characterisation of the boron nitride layers, we performed aberration-corrected scanning transmission electron microscopy combined with electron energy loss spectroscopy (AC-STEM-EELS) core-loss hyperspectral imaging on individual nanotubes. All experiments were carried out using a Nion UltraSTEM operated at 60 keV with a convergence semi-angle of 30 mrad.

2.2.2. X-ray photoemission spectroscopy (XPS). XPS measurements acquired using a Kratos Axis Ultra spectrometer with a monochromated Al Kα X-ray source ($h\nu$ = 1486.7 eV). Photoelectrons were collected by the analyser at a pass energy of 160 eV for survey scans, and 20 eV for high-resolution core level scans. Charge compensation was provided by flooding the surface with 3 eV electrons. The binding energy scale was calibrated by a rigid shift to align the C 1s binding energy of adventitious carbon to 285 eV. XPS data were analysed using the CasaXPS software package.[24]

2.2.3. Atomic force microscopy (AFM). Surface morphology of the nanotubes was analysed by Atomic Force Microscopy (AFM) using an Asylum Cypher S (Oxford Instruments) microscope. Images were acquired in tapping mode using NuNano SCOUT 70 RAl probes (nominal spring constant 2 N m^{-1}). AFM images were processed and analysed using the Gwyddion software package.[25]

2.2.4. Variable angle spectroscopic ellipsometry (VASE). VASE measurements on the sapphire surface close to the MWCNTs were carried out after HT-MBE using an Accurion EP4 imaging spectroscopic ellipsometer (iSE) at wavelengths from 190–1000 nm and a 50° angle of incidence. The areas analysed were approximately 100 μm × 100 μm^2 in area, and at a location a few hundred microns from the bundles of carbon nanotubes. Measurements on the nanotubes themselves were not possible due to the high light scattering from the bundles of nanotubes.

2.2.5. **Photoluminescence (PL) cryomicroscopy.** Investigation of the opto-electronic properties of our quasi-one-dimensional (1D) BN nanoribbons (BNNRs) wrapped around CNTs was performed by means of a home-made scanning confocal cryomicroscope (8 K) with an achromatic design allowing PL measurements with a spatial resolution given by the diffraction limit in the UV-C range, at wavelengths ~200 nm (~6 eV).[26]

3. Results and discussion

We first verify hBN growth on the nanotubes using XPS. Spectra in Fig. 1a–c were acquired at different positions on the sample that contained dense MWCNTs (red spectra) and on the surface away from MWCNTs (blue spectra), noting that it was not possible to avoid the MWCNTs altogether. Both regions show strong N 1s (398.1 eV) and B 1s (190.5 eV) signals with π–π* shake up features confirming the formation of sp^2 hBN on the MWCNTs and on the sapphire substrate.[27] The B 1s spectrum acquired on the MWCNTs also shows a clear low-binding component corresponding to C–B bonding,[28] with the signal also seen in the C 1s core level. There is also a slight asymmetry to the N 1s core level, which could be due to C–N bonding,[28] but this is not easily verifiable from the C 1s core level, as C–N bonds and C–O bonds from adventitious carbon can have a similar binding energy range. The C 1s core level shows a distinctly different line shape on and off the nanotubes owing to the sp^2 bonding in MWCNTs (narrow, asymmetric peak) and sp^3 bonding in adventitious carbon (broader, symmetric peak). Complete peak deconvolution of the hBN/MWCNT/sapphire is shown in Fig. S1. Neither C–B nor C–N bonding was able to be identified in hBN on sapphire, suggesting that these components could arise due to interfacial bonding at the end caps of the MWCNTs, or defects on the MWCNT surface. We note that due to the high temperature growth conditions that it feasible to produce B–C and N–C by substitutional doping of the nanotubes. In previous studies of

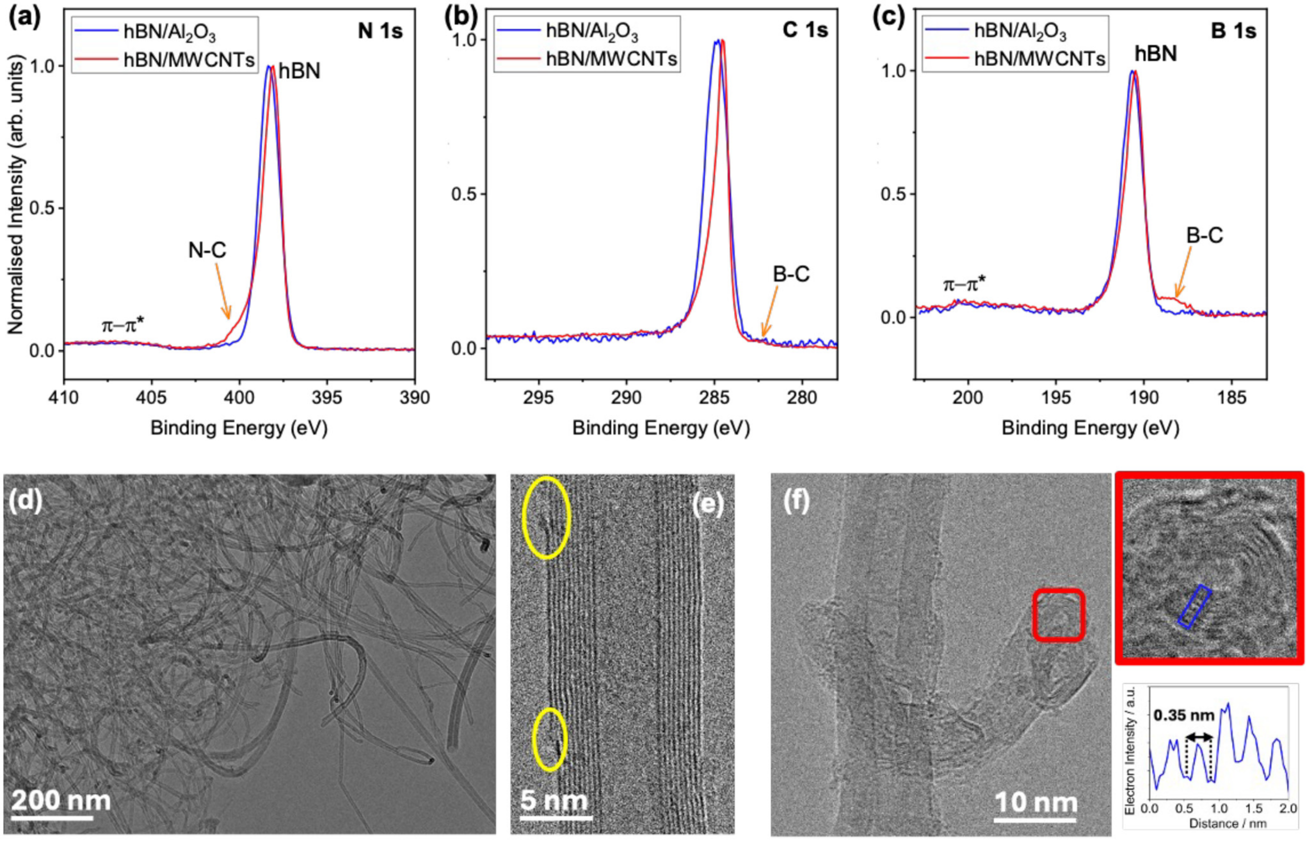

Fig. 1 High-resolution XP spectra of the (a) N 1s, (b) C 1s and (c) B 1s core levels of the hBN layers grown on MWCNTs on sapphire supporting substrates. Red and blue spectra correspond to measurements acquired on MWCNT and sapphire regions, respectively. (d) A large field of view TEM image illustrating the distribution of nanotubes on a TEM grid. (e) High-magnification HRTEM image of an individual carbon nanotube with defect sites (yellow circles). (f) HRTEM image of a boron nitride structure grown on top of a carbon nanotube. A magnified area in (e) demonstrating the concentric tubular nature of some boron nitride structures is indicated by the red box, with the intensity line profile (underneath) revealing a repeating distance between the layers corresponding to the van der Waals gap.

hBN grown on HOPG substrates, we have not observed these chemical species in laboratory- or synchrotron-based photoemission spectra.[7,27] Hence, we speculate that the B–C and N–C species arise from interfacial bonding at the ends of the MWCNTs or surface defects.

Atomic force microscopy of the MWCNTs before and after hBN growth by HT-MBE clearly show changes in the surface morphology (see Fig. S2 and associated discussion). Due to tip-induced artefacts and limitations to the spatial resolution, it is not possible to attain a full structural characterisation of the hBN/MWCNTs. We have therefore used high-resolution transmission electron microscopy (HR-TEM) to analyse individual nanotubes. Nanotubes that have been exposed to HT-MBE growth of boron nitride revealed MWCNTs with a similar appearance to that of pristine MWCNTs (Fig. 1d). The nanotubes still had an interwall spacing of 0.335 nm, close to the expected graphitic distance. Additionally, no large particles of B or BN were seen throughout the sample. Closer inspection of individual nanotubes revealed multiple occurrences where the outer wall of the MWCNTs appeared to terminate in a defect (yellow circles, Fig. 1e), or cases where the MWCNTs possessed an uneven number of walls on either side (Fig. 1e). Nanotubes were also found in a 'corkscrew' configuration, with a smaller nanotube wrapped around a larger one, a structure not observed in pristine MWCNTs. Scanning transmission electron microscopy-energy dispersive X-ray (STEM-EDX) analysis (Fig. S3) showed nitrogen signal throughout the sample, but with an increase in nitrogen content in areas where the termini of multiple MWCNTs overlapped.

Bright-field TEM shows fringes that are indicative of wrapping of the nanotubes with hBN, rather than deposition of particles. There are also features that are atypical of carbon nanotubes, *e.g.* end-on 'welding' of the nanotubes, as demonstrated by black spots in Fig. 1d. TEM imaging reveals that the nanotubes after boron nitride growth on MWCNT retain their cylindrical appearance and high aspect ratio (Fig. S3a). STEM and STEM-EDX elemental mapping reveal carbon and nitrogen along the nanotube structures, with nitrogen originating from the formation of boron nitride on the carbon nanotubes (Fig. S3b and c). High-resolution TEM of selected areas show a system of interconnected nanostructures, consistent with hybrid hBN wrapped MWCNT (Fig. S3d and e).

In order to better understand the structure and chemistry of the hBN growth on MWCNTs, we performed aberration-corrected STEM-EELS (AC-STEM-EELS) analysis of individual nanotubes. TEM imaging of other areas of the sample shows a consistently similar sample morphology (Fig. S3 and S4a, b). In some areas, STEM imaging at high magnification reveals unusual structures formed on the outside of the carbon nanotube (Fig. S4c). STEM-EDX mapping detects signals from both carbon and boron, with the latter arising from the grown boron nitride structures (Fig. S4d and e). Electron energy-loss spectroscopy (EELS) of this area shows a boron K-edge (Fig. S4f), confirming the presence of sp^2 boron nitride in the features grown on carbon nanotubes during the MBE process, as seen in TEM and STEM images.

Fig. 2a displays a high-angle annular dark-field (HAADF) image of a typical coated carbon nanotube. The corresponding EELS elemental maps for boron, carbon, and nitrogen are shown in Fig. 2b–d, and a composite map is presented in Fig. 2e. The layered structure of the nanotube is clearly resolved in both the HAADF image and the chemical maps. The strong spatial correlation between the boron and nitrogen signals, together with the characteristic core-loss fine structure (extracted from Region A in Fig. 2f), unambiguously identifies the sp^2 character of hBN.

The overall structure can be described as a coaxial heterostructure comprising an inner multiwalled carbon nanotube coated with a few thin hBN layers (green and purple for C and BN, respectively; Fig. 3e). As evidenced in the boron map, the coverage is partial and organised into BN patches. In Fig. 2g, the integrated line profile of region B in Fig. 2e reveals regularly spaced layers with an interlayer distance of ∼3.3 Å, indicating that the hBN coverage can be as thin as a single monolayer. Thicker regions are also observed (*e.g.*, Region A), corresponding to two-layer hBN domains. However, in all nanotubes examined, no thick hBN growth was observed; the number of BN monolayers typically ranges from one to three.

We have used different growth times for boron nitride on CNTs, 2 and 4 h. For the samples grown for 2 hours presented in Fig. 2, the B and N maps have an uneven intensity, indicating that the hBN layer is not uniform. The intensity profiles in Fig. 2g clearly indicate that the hBN coating is one monolayer thick in some areas and two monolayers thick in others. Fig. S5 presents the results of the longer growth run, where the growth time was increased to 4 hours. Fig. S5 demonstrates more uniform coverage of boron nitride on the external surfaces of carbon nanotubes. The B and N signals are perfectly spatially correlated and appear outside the carbon inner core of the CNTs. The included image allows for precise measurement of the distance between the peaks in the carbon and boron nitride signals. Fig. 2 and S5 suggest that what we see are the results of the step-flow mechanism of hBN monolayer growth around the carbon nanotube surface, which we can call the "wrapping" mechanism. In Fig. 2, we observe two monolayers of the wrap on one side of the CNT and only one on the other. After initial nucleation, the lateral growth front of the hBN monolayer moves in a step-flow mode around the surface of the CNT. Thus far we have been unable to determine unequivocally whether the hBN layers coalesce into nanotubes or continue to form nanoscrolls. Unfortunately, at this stage, we cannot draw any conclusions about the mechanisms of initial nucleation of boron nitride on the flat surfaces of CNTs; we can only speculate that such nucleation is promoted by the deposition of boron on structural point defects.

Previously, we observed growth of hBN nucleating preferentially along step edges on HOPG substrates.[9] It is therefore interesting to consider how hBN growth evolves from the open ends of the MWCNTs which contain analogous edges. Fig. 3a shows a HAADF-AC-STEM image of a MWCNT tip following hBN growth, and the corresponding AC-STEM-EELS elemental maps are shown in Fig. 3b–f, and a composite map in Fig. 3f.

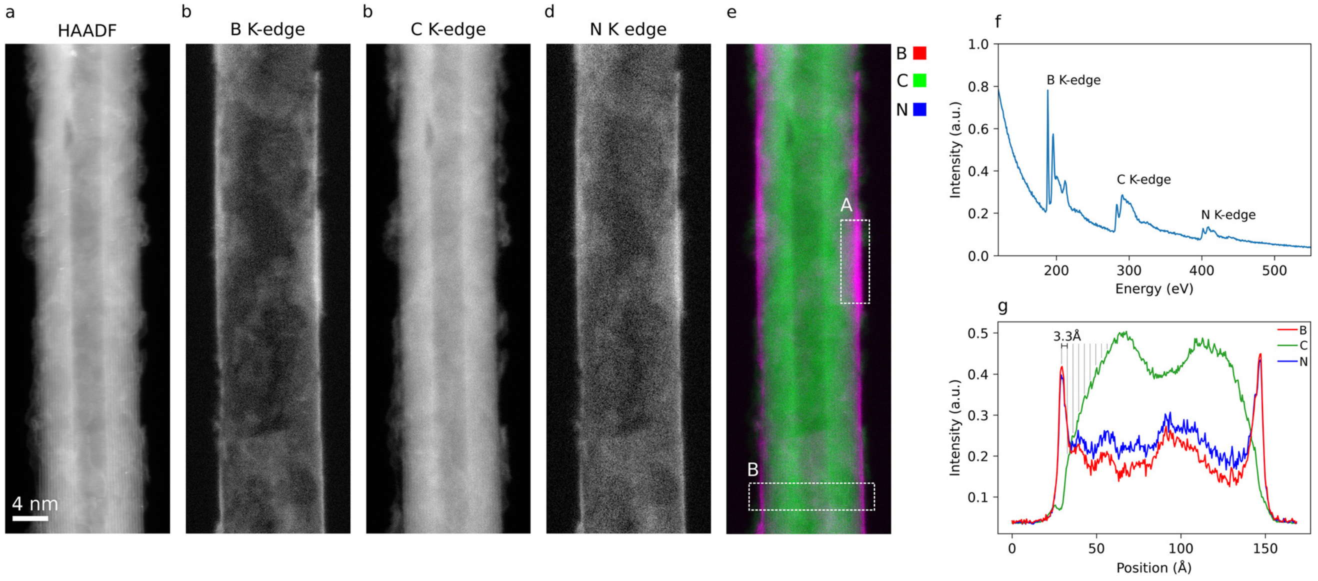

Fig. 2 STEM-EELS analysis of the MWCNTs after HT-MBE of boron nitride for 2 hours. (a) High angle annular dark field image (b–d) elemental maps extracted from integration of the B, C and N K-edges, respectively. (e) Composed elemental map. (f) Core-EELS spectrum integrated over the A region of (f). (g) Line profiles of the elemental maps extracted along region B.

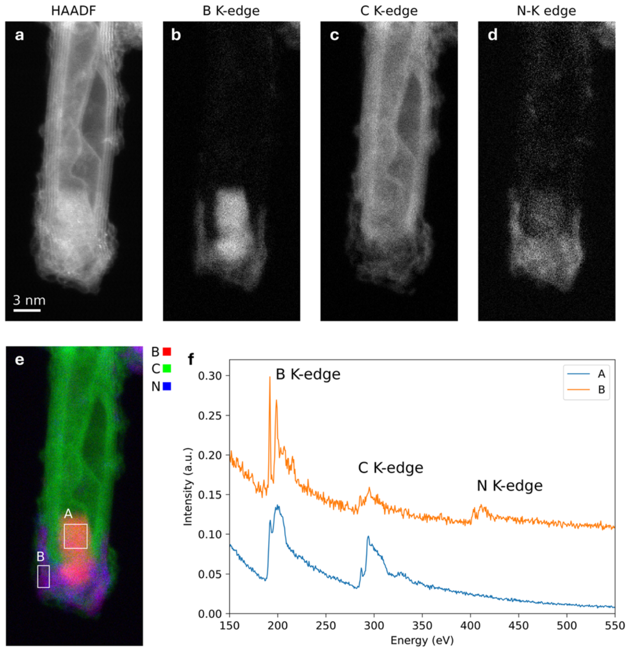

Fig. 3 STEM-EELS analysis of the MWCNTs after HT-MBE of boron nitride for 2 hours. (a) High angle annular dark field image (b–d) elemental maps extracted from integration of the B, C and N K-edges, respectively. (e) Composed elemental map. (f) Core-EELS spectrum integrated over the A and B regions of (e).

These maps demonstrate, firstly, that the MWCNT has been partially filled with elemental boron. Additional, coincident B and N signals on the end cap with the absence of a strong C signal demonstrate the formation of a lateral, circular heterojunction between the MWCNT and a small BNNT end cap. These assignments are confirmed by the EELS spectra in Fig. 3f, where the signal from region A, corresponding to the boron ‘plug’, shows only the B and C K-edges, whereas region B, corresponding to the BNNT cap, shows B and N K-edges and only a weak C K-edge. Furthermore, the EELS spectra confirm the sp^2 character of hBN for the end cap. The B K-edge of the ‘plug’ shows a distinct fine structure to the BNNT cap, and more closely resembles that of elemental boron.[29]

It appears that there is also a good lateral junction between the outer two monolayers of carbon nanotube and the grown BN monolayers. It confirms that we have epitaxial lateral growth of BN from the open step edges of the carbon nanotube, aligning well with our expectations and previous results. We believe that boron adatoms must be very mobile at our epitaxial temperatures of 1390 °C, which allows boron atoms to diffuse on both the external and the internal surface of CNTs and to accumulate boron close to the tip. Recently, we have demonstrated the possibility of HT-MBE growth of high-quality monolayer thick boron nitride-graphene-boron nitride lateral heterostructures on the surface of HOPG substrates.[9,16,30] This is a result of a good lattice match between graphene and hBN. Here we have a similar lateral heterojunction, but at the edge of a round circular tip of the carbon nanotube. We are currently considering potential practical applications for such a new type of circular lateral CNTs – BNNTs heterojunctions.

Using AC-STEM-EELS analysis, we have also explored nanotubes in a “corkscrew” configuration observed previously by TEM in Fig. 1f. Fig. S6 presents an example of such a “corkscrew” nanotube in the sample grown for 4 hours. The core of the nanotube consists of carbon, and the outer shell is formed by boron nitride. Therefore, this is also a coaxial heterostructure consisting of an inner multiwalled carbon nanotube coated with a few thin hBN monolayers, but with these nanotubes somehow twisted around other CNTs, forming such a "corkscrew" appearance, which we did not observe in the initial CNTs. This behaviour is likely related to strain in the carbon-BN heterostructures, and the tendency of BNNTs form kinks rather than bend like CNTs, which led to their twisting around other nanotubes.

To probe the optical characteristics of the hBN/MWCNT structures we first used spectroscopic ellipsometry measurements after boron nitride growth show that the hBN layer on sapphire in the areas away from CNTs is around 6 ± 2 nm thick. This is significantly thicker than the hBN on the carbon nanotubes, as shown in Fig. 2 and S5. That agrees with our earlier studies, which demonstrated that the hBN layers grown on sapphire by HT-MBE grow faster than on HOPG.[31]

To distinguish the optical properties of the hBN/MWCNTs and hBN/sapphire we have used PL cryomicroscopy. Fig. 4a shows PL mapping of the emission spectrally integrated between 5.5 and 6 eV, close to the band-edge of hBN, at the border of the CNTs deposited on the sapphire (Sa) substrate. A significant ~2.5 fold-enhancement of the PL signal intensity at ~5.7 eV occurs when the excitation laser spot is located on the CNTs with respect to the bare sapphire substrate. The PL spectra detected in 2 × 2 μm^2 regions either on the CNTs aggregates or on sapphire (black and red squares in panel a, respectively) reveal substantial differences not only above 5 eV but also close to 4 eV in the spectral range of emission of the carbon dimer in hBN.[32] The PL spectrum recorded on sapphire displays an intense broad band centred at ~3.8 eV, mostly coming from residual PL from sapphire, while no bright emission is recorded above 5 eV, close to the band-edge of hBN. This observation agrees with previous reports on the optical properties of hBN epitaxially grown on sapphire by MBE at the same substrate temperature of 1390 °C.[31] For the epitaxy of hBN on sapphire, higher growth temperatures up to 1690 °C increased the UV-C emission of hBN, suggesting improved hBN crystal quality. Conversely, a sapphire temperature of 1390 °C does not provide favourable epitaxial conditions for hBN, as confirmed by our PL measurements in Fig. 4b. The opposite phenomenology was reported for the MBE growth of hBN on HOPG, the lowest substrate temperature of 1390 °C bringing the most intense UV-C emission of epitaxial hBN.[31] Interestingly, in the present case of the hBN deposition on CNTs of intrinsically the same graphitic structure as HOPG, an intense emission above 5 eV is recorded (black line, Fig. 4b). In order to better visualise the PL signal specifically detected on the CNTs, we plot in blue line in Fig. 4c the difference between the PL spectra of Fig. 4b. Fine structures at 5.43, 5.66 and 5.84 eV are resolved together with a multiplet at ~6 eV, which is not PL but resonant Raman scattering.[33] In this reference, it was demonstrated that under quasi-resonant laser excitation, the UV-C emission of monolayer hBN on HOPG consists of resonant Raman scattering and PL, the former giving rise to a multiplet shifting with the laser energy, the latter being centred at ~6.045 eV, *i.e.* the direct exciton energy in direct-gap monolayer hBN.[33] In the present PL experiments under laser excitation at 6.358 eV, the expected multiplet of resonant Raman scattering is plotted as the black line in Fig. 4c, and it exactly matches the fine structure at ~6 eV (shaded area in Fig. 4c), which can thus be excluded from our discussion of the PL spectrum of the quasi-1D hBN epitaxially grown around the MWCNTs. Remarkably, the UV-C PL of our hBN features components at energies as high as 5.84 eV, which are totally absent from the emission spectra of state-of-the-art few-wall BNNTs coming from two reference samples (orange and green lines in Fig. 4c). Such spectra correspond to the typical spectrum of excitons loca-

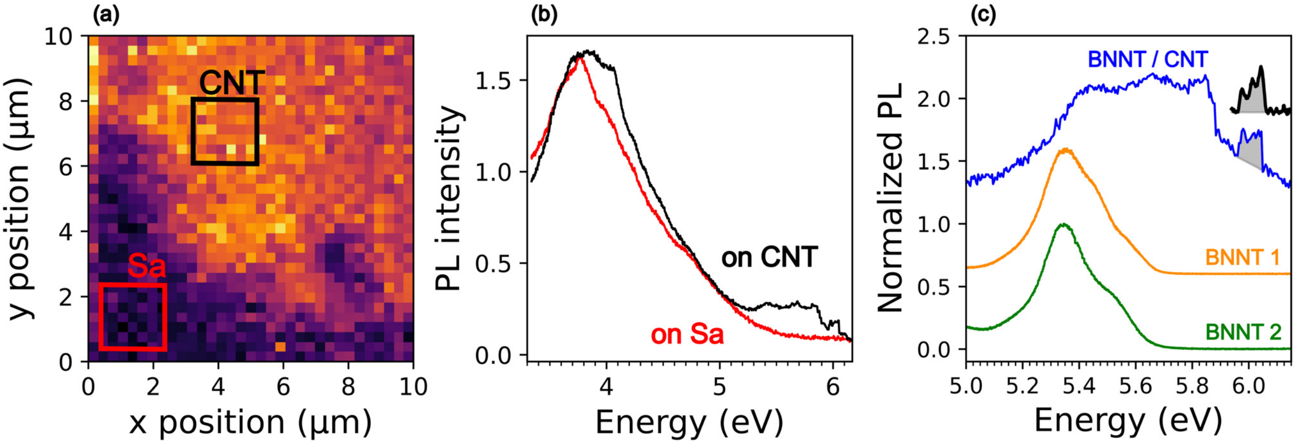

Fig. 4 Hyperspectral imaging of hBN in a 10 × 10 μm^2 area at the border of the CNT aggregates deposited on the sapphire (Sa) substrate, at 8 K, for an excitation energy of 6.358 eV (λ ~195 nm). (a) Emission intensity map spectrally integrated between 5.5 and 6 eV, (b) emission spectra at two different locations, either on the bare sapphire substrate ('on Sa'), or on the CNTs aggregates ('on CNT'), indicated by the red and black squares in panel (a), respectively. (c) The difference of the spectra plotted in panel (b) is plotted in a blue line, and compared to the spectra recorded in two reference samples of few wall-BNNTs (BNNT1 – from BNNT LLC, USA, product "SP10RX Powder", BNNT2 from Tekna Holdings Canada Inc.).

lized at extended defects in hBN.[34] The line around 5.8 eV in the PL spectrum of the hBN/MWCNTs is similar to the phonon replica in bulk hBN related to phonon-assisted recombination involving optical phonons.[1,31] To the best of our knowledge, such a PL spectrum is the first evidence for intrinsic radiative recombination of excitons in quasi-1D hBN, with an indirect bandgap estimated at ~5.95 eV. Because the present BNNTs wrapped around CNTs are made of a few monolayers, the question of the stacking order arises for this novel quasi-1D form of layered hBN. In this context, the emission energy of the carbon dimer has been identified as a sensitive probe of the stacking sequence.[35] In hBN in the standard AA′ stacking, a well-defined zero-phonon line is observed at low temperature at an energy of ~4.098 eV, while the AB-stacking leads to two inequivalent configurations of the carbon dimer with two zero-phonon lines at 4.146 and 4.161 eV, and rhombohedral BN, often described in terms of an ABC stacking, shows one zero-phonon line at 4.143 eV.[36] In the present case, the emission around 4 eV looks similar to the emission spectrum of the carbon dimer but with a broad zero-phonon line which cannot be precisely characterized, the emission around 4 eV being most probably dominated by the low-energy acoustic phonon sideband.[37] Its maximum occurs at an energy of ~4.057 eV which is ~30 meV lower than in the reference case of the carbon dimer in AA'-stacked hBN. The origin of the shift relative to reference samples is not yet well understood. We consider two points of difference here compared to the reference case: (1) moiré effects arising from the difference in hBN and MWCNT lattice constants, (2) the presence of strain between hBN and MWCNTs due to moiré effects and bending of the layer around the nanotube. The relationship between moiré periodicity and strain in heterostructures of graphene and hBN grown by HT-MBE have been extensively studied the past.[38] We expect a moiré period of ~14 nm due to the lattice mismatch alone but have previously observed larger moiré periods, up to 18.3 nm, in hBN/HOPG corresponding to compressive strains up to 0.5% in the hBN layer.[14] These moiré periods result in local modulation of the electronic structure which may cause broadening of excitonic features in optical spectra but are not expected to be the cause of the redshift.[14] Strain may account for a shift of the deep level emission, but we note that the response of different emitters to strain can vary.[39,40] We also cannot exclude bandgap renormalisation effects due to proximity to the MWCNTs.[41] Overall, this significant red shift may provide important information for future *ab initio* calculations of the opto-electronic properties of our few-layer hBN synthesised by HT-MBE around MWCNTs.

4. Conclusions

We have demonstrated HT-MBE as a route to creating novel quasi-1D heterostructures of hBN and MWCNTs. Our in-depth structural analysis demonstrates growth on both the external surface, and opened tips of the MWCNTS, forming coaxial and lateral heterojunctions, respectively. The high structural quality of HT-MBE on the graphitic surface of MWCNTs enables us to probe the optoelectronic characteristics of quasi-1D hBN. We observe evidence of intrinsic radiative exciton recombination which is not present in pure BNNTs. These results position HT-MBE as a unique route to explore the electronic and optical properties of quasi-1D hBN/MWCNT heterojunctions.

Author contributions

Jonathan Bradford: methodology (AFM, XPS), investigation (AFM, XPS), formal analysis (XPS, AFM), writing (original draft, review & editing); William. J. Cull: methodology (TEM), investigation (TEM), formal analysis (TEM), writing (original draft, review & editing); Tin S. Cheng: methodology (MBE), investigation (MBE), writing (review & editing); Amy F. M. Collins: investigation (AFM), writing (review & editing); Christopher J. Mellor: methodology (VASE), investigation (VASE), formal analysis (VASE), writing (review & editing), supervision; Andrei N. Khlobystov: methodology (TEM), supervision, writing (review & editing); Alberto Zobelli: methodology (AC-STEM), investigation (AC-STEM), writing (review & editing); Alexandre Gloter: methodology (AC-STEM), investigation (AC-STEM), writing (review & editing); Alexandra Ibanez: investigation (UV-PL), writing (review & editing); Bernard Gil: methodology (UV-PL), writing (review & editing); Pierre Valvin: methodology (UV-PL), investigation (UV-PL); Guillaume Cassabois: methodology (UV-PL), investigation (UV-PL), writing (review & editing); Sergei V. Novikov: conceptualisation, methodology (MBE), funding acquisition, supervision, writing (original draft, writing & editing).

Conflicts of interest

There are no conflicts to declare.

Data availability

The data supporting this article have been included in the paper and the supplementary information (SI). Supplementary information is available. See DOI: https://doi.org/10.1039/d6nr01376g.

Acknowledgements

This work at Nottingham was supported by the Engineering and Physical Sciences Research Council UK (Grant No. EP/V05323X/1, EP/W035510/1, EP/V000055/1, EP/K005138/1, EP/W006413/1) and the Leverhulme Trust, grant number RPG-2022-300. The authors thank the Nanoscale and Microscale Research Centre (nmRC) for providing access to instrumentation. This work at Laboratoire Charles Coulomb-Montpellier, France was financially supported by the

BONASPES (No. ANR-19-CE30-0007), and HETEROBNC (No. ANR20-CE09-0014-02) projects.

References

1 G. Cassabois, P. Valvin and B. Gil, *Nat. Photonics*, 2016, **10**(4), 262–266.

2 J. D. Caldwell, I. Aharonovich, G. Cassabois, J. H. Edgar, B. Gil and D. N. Basov, *Nat. Rev. Mater.*, 2019, **4**(8), 552–567.

3 I. Aharonovich, J.-P. Tetienne and M. Toth, *Nano Lett.*, 2022, **22**, 9227–9235.

4 T. T. Tran, K. Bray, M. J. Ford, M. Toth and I. Aharonovich, *Nat. Nanotechnol.*, 2016, **11**, 37–41.

5 C. R. Dean, A. F. Young, I. Meric, C. Lee, L. Wang, S. Sorgenfrei, K. Watanabe, T. Taniguchi, P. Kim, K. L. Shepard and J. Hone, *Nat. Nanotechnol.*, 2010, **5**, 722–726.

6 A. K. Geim and I. V. Grigorieva, *Nature*, 2013, **499**, 419–425.

7 Y.-J. Cho, A. Summerfield, A. Davies, T. S. Cheng, E. F. Smith, C. J. Mellor, A. N. Khlobystov, C. T. Foxon, L. Eaves, P. H. Beton and S. V. Novikov, *Sci. Rep.*, 2016, **6**, 34474.

8 T. S. Cheng, A. Summerfield, C. J. Mellor, A. Davies, A. N. Khlobystov, L. Eaves, C. T. Foxon, P. H. Beton and S. V. Novikov, *J. Vac. Sci. Technol., B:Nanotechnol. Microelectron.: Mater., Process., Meas., Phenom.*, 2018, **36**, 02D103.

9 J. Wrigley, J. Bradford, T. James, T. S. Cheng, J. Thomas, C. J. Mellor, A. N. Khlobystov, L. Eaves, C. T. Foxon, S. V. Novikov and P. H. Beton, *2d Mater.*, 2021, **8**, 034001.

10 J. Bradford, A. F. M. Collins, T. S. Cheng, J. Shen, J. Kerfoot, G. A. Rance, J. Li, C. J. Mellor, P. H. Beton, G. Cassabois, S. Dai, J. H. Edgar and S. V. Novikov, *npj 2D Mater. Appl.*, 2025, **9**, 98.

11 C. Elias, P. Valvin, T. Pelini, A. Summerfield, C. J. Mellor, T. S. Cheng, L. Eaves, C. T. Foxon, P. H. Beton, S. V. Novikov, B. Gil and G. Cassabois, *Nat. Commun.*, 2019, **10**, 2639.

12 K. Shima, T. S. Cheng, C. J. Mellor, P. H. Beton, C. Elias, P. Valvin, B. Gil, G. Cassabois, S. V. Novikov and S. F. Chichibu, *Sci. Rep.*, 2024, **14**(1), 169.

13 R. J. P. Román, F. J. R. C. Costa, A. Zobelli, C. Elias, P. Valvin, G. Cassabois, B. Gil, A. Summerfield, T. S. Cheng, C. J. Mellor, P. H. Beton, S. V. Novikov and L. F. Zagonel, *2d Mater.*, 2021, **8**, 044001.

14 F. J. R. Costa, D. Arribas, T. G. L. Brito, T. S. Cheng, J. Bradford, A. Thompson, A. Saywell, C. J. Mellor, P. H. Beton, S. V. Novikov, J. Plo, B. Gil, G. Cassabois, L. F. Zagonel, K. Kuhnke, K. Kern and A. Rosławska, *ACS Nano*, 2025, **19**, 35528–35538.

15 N. Mendelson, D. Chugh, J. R. Reimers, T. S. Cheng, A. Gottscholl, H. Long, C. J. Mellor, A. Zettl, V. Dyakonov, P. H. Beton, S. V. Novikov, C. Jagadish, H. H. Tan, M. J. Ford, M. Toth, C. Bradac and I. Aharonovich, *Nat. Mater.*, 2021, **20**, 321–328.

16 J. Thomas, J. Bradford, T. S. Cheng, A. Summerfield, J. Wrigley, C. J. Mellor, A. N. Khlobystov, C. T. Foxon, L. Eaves, S. V. Novikov and P. H. Beton, *2d Mater.*, 2020, **7**, 035014.

17 R. S. Jones, B. Maciejewska and N. Grobert, *Nanoscale Adv.*, 2020, **2**, 4996–5014.

18 K. Chen, C. Yu, X. Wang, S. Zhou, L. Wang, Y. Qu, A. Wang, F. Xiao, Z. Li, C. Li, J. Dai, X. Wan, R. Lu and Q. Dai, *Nat. Mater.*, 2025, **24**, 1773–1777.

19 W. J. Cull, Q. M. Ramasse, J. Biskupek, G. A. Rance, I. Cardillo-Zallo, B. L. Weare, M. W. Fay, R. R. Whitney, L. R. Scammell, J. A. Fernandes, U. Kaiser, A. Patanè and A. N. Khlobystov, *Adv. Mater.*, 2025, **37**, 2501821.

20 J. K. Qin, P. Y. Liao, M. Si, S. Gao, G. Qiu, J. Jian, Q. Wang, S. Q. Zhang, S. Huang, A. Charnas, Y. Wang, M. J. Kim, W. Wu, X. Xu, H. Y. Wang, L. Yang, Y. Khin Yap and P. D. Ye, *Nat. Electron.*, 2020, **3**(3), 141–147.

21 I. Cardillo-Zallo, J. Biskupek, S. Bloodworth, E. S. Marsden, M. W. Fay, Q. M. Ramasse, G. A. Rance, C. T. Stoppiello, W. J. Cull, B. L. Weare, R. J. Whitby, U. Kaiser, P. D. Brown and A. N. Khlobystov, *ACS Nano*, 2024, **18**, 2958–2971.

22 W. J. V. Townsend, D. López-Alcalá, M. A. Bird, J. W. Jordan, G. A. Rance, J. Biskupek, U. Kaiser, J. J. Baldoví, D. A. Walsh, L. R. Johnson, A. N. Khlobystov and G. N. Newton, *Nat. Commun.*, 2025, **16**, 4460.

23 K. E. Walker, G. A. Rance, Á. Pekker, H. M. Tóháti, M. W. Fay, R. W. Lodge, C. T. Stoppiello, K. Kamarás and A. N. Khlobystov, *Small Methods*, 2017, **1**, 1700184.

24 N. Fairley, V. Fernandez, M. Richard-Plouet, C. Guillot-Deudon, J. Walton, E. Smith, D. Flahaut, M. Greiner, M. Biesinger, S. Tougaard, D. Morgan and J. Baltrusaitis, *Appl. Surf. Sci. Adv.*, 2021, **5**, 100112.

25 D. Nečas and P. Klapetek, *Open Phys.*, 2012, **10**, 181–188.

26 P. Valvin, T. Pelini, G. Cassabois, A. Zobelli, J. Li, J. H. Edgar and B. Gil, *AIP Adv.*, 2020, **10**, 75025.

27 D. Pierucci, J. Zribi, H. Henck, J. Chaste, M. G. Silly, F. Bertran, P. Le Fevre, B. Gil, A. Summerfield, P. H. Beton, S. V. Novikov, G. Cassabois, J. E. Rault and A. Ouerghi, *Appl. Phys. Lett.*, 2018, **112**, 253102.

28 S. Nappini, I. Píš, G. Carraro, E. Celasco, M. Smerieri, L. Savio, E. Magnano and F. Bondino, *Carbon*, 2017, **120**, 185–193.

29 D. Golberg, P. M. F. J. Costa, O. Lourie, M. Mitome, X. Bai, K. Kurashima, C. Zhi, C. Tang and Y. Bando, *Nano Lett.*, 2007, **7**, 2146–2151.

30 J. Bradford, T. S. Cheng, T. S. S. James, A. N. Khlobystov, C. J. Mellor, K. Watanabe, T. Taniguchi, S. V. Novikov and P. H. Beton, *2d Mater.*, 2023, **10**, 035035.

31 T. Q. P. Vuong, G. Cassabois, P. Valvin, E. Rousseau, A. Summerfield, C. J. Mellor, Y. Cho, T. S. Cheng, J. D. Albar, L. Eaves, C. T. Foxon, P. H. Beton, S. V. Novikov and B. Gil, *2d Mater.*, 2017, **4**, 021023.

32 J. Plo, A. Pershin, S. Li, T. Poirier, E. Janzen, H. Schutte, M. Tian, M. Wynn, S. Bernard, A. Rousseau, A. Ibanez, P. Valvin, W. Desrat, T. Michel, V. Jacques, B. Gil,

A. Kaminska, N. Wan, J. H. Edgar, A. Gali and G. Cassabois, *Phys. Rev. X*, 2025, **15**, 021045.

33 A. Rousseau, J. Plo, P. Valvin, T. S. Cheng, J. Bradford, T. S. S. James, J. Wrigley, C. J. Mellor, P. H. Beton, S. V. Novikov, V. Jacques, B. Gil and G. Cassabois, *2d Mater.*, 2024, **11**, 025026.

34 G. Cassabois, P. Valvin and B. Gil, *Phys. Rev. B*, 2016, **93**, 035207.

35 A. Rousseau, P. Valvin, C. Elias, L. Xue, J. Li, J. H. Edgar, B. Gil and G. Cassabois, *Phys. Rev. Mater.*, 2022, **6**, 094009.

36 W. Desrat, M. Moret, J. Plo, T. Michel, A. Ibanez, P. Valvin, V. Jacques, I. Philip-Robert, G. Cassabois and B. Gil, *Phys. Rev. Mater.*, 2025, **9**, 124001.

37 T. Q. P. Vuong, G. Cassabois, P. Valvin, A. Ouerghi, Y. Chassagneux, C. Voisin and B. Gil, *Phys. Rev. Lett.*, 2016, **117**, 097402.

38 A. Davies, J. D. Albar, A. Summerfield, J. C. Thomas, T. S. Cheng, V. V. Korolkov, E. Stapleton, J. Wrigley, N. L. Goodey, C. J. Mellor, A. N. Khlobystov, K. Watanabe, T. Taniguchi, C. T. Foxon, L. Eaves, S. V. Novikov and P. H. Beton, *Nano Lett.*, 2018, **18**, 498–504.

39 X. Chen, X. Yue, L. Zhang, X. Xu, F. Liu, M. Feng, Z. Hu, Y. Yan, J. Scheuer and X. Fu, *Adv. Funct. Mater.*, 2024, **34**, 2306128.

40 T. Yang, P. Huang, Z. Qiu, Y. Han, D. Guan, P. Lyu, J. Su, K. S. Novoselov, H. Fang and J. Lu, *ACS Nano*, 2026, **20**, 10594–10604.

41 P. Wang, W. Lee, J. P. Corbett, W. H. Koll, N. M. Vu, D. A. Laleyan, Q. Wen, Y. Wu, A. Pandey, J. Gim, D. Wang, D. Y. Qiu, R. Hovden, M. Kira, J. T. Heron, J. A. Gupta, E. Kioupakis and Z. Mi, *Adv. Mater.*, 2022, **34**, 2201387.